Volumetric sub-surface imaging using spectrally encoded endoscopy

D. Yelin,[1*] B. E. Bouma,[2] and G. J. Tearney[3]

[1]*Department of Biomedical Engineering, Technion – Israel Institute of Technology, Haifa 32000, Israel*

[2]*Harvard Medical School and the Wellman Center for Photomedicine, Massachusetts General Hospital, 55 Fruit Street, BAR 703, Boston, Massachusetts 02114*

[3]*Harvard Medical School, Wellman Center for Photomedicine, and the Pathology Department, Massachusetts General Hospital, 55 Fruit Street, BAR 703, Boston, Massachusetts 02114*

Corresponding author: yelin@bm.technion.ac.il

Abstract: Endoscopic imaging below tissue surfaces and through turbid media may provide improved diagnostic capabilities and visibility in surgical settings. Spectrally encoded endoscopy (SEE) is a recently developed method that utilizes a single optical fiber, miniature optics and a diffractive grating for high-speed imaging through small diameter, flexible endoscopic probes. SEE has also been shown to provide three-dimensional topological imaging capabilities. In this paper, we have configured SEE to additionally image beneath tissue surfaces, by increasing the system's sensitivity and acquiring the complex spectral density for each spectrally resolved point on the sample. In order to demonstrate the capability of SEE to obtain subsurface information, we have utilized the system to image a resolution target through intralipid solution, and conduct volumetric imaging of a mouse embryo and excised human middle-ear ossicles. Our results demonstrate that real-time subsurface imaging is possible with this miniature endoscopy technique.

References and Links

1. E. Montgomery, M. P. Bronner, J. R. Goldblum, J. K. Greenson, M. M. Haber, J. Hart, L. W. Lamps, G. Y. Lauwers, A. J. Lazenby, D. N. Lewin, M. E. Robert, A. Y. Toledano, Y. Shyr, and K. Washington, "Reproducibility of the diagnosis of dysplasia in Barrett esophagus: A reaffirmation," Human Pathology **32**, 368-378 (2001).
2. C. Klug, B. Fabinyi, and M. Tschabitscher, "Endoscopy of the middle ear through the Eustachian tube: Anatomic possibilities and limitations," Am. J. Otol. **20**, 299-303 (1999).
3. M. A. D'Hallewin, S. El Khatib, A. Leroux, L. Bezdetnaya, and F. Guillemin, "Endoscopic confocal fluorescence microscopy of normal and tumor bearing rat bladder," J. Urol. **174**, 736-740 (2005).
4. A. F. Gmitro, and D. Aziz, "Confocal Microscopy through a Fiberoptic Imaging Bundle," Opt. Lett. **18**, 565-567 (1993).
5. C. Liang, K. B. Sung, R. R. Richards-Kortum, and M. R. Descour, "Design of a high-numerical-aperture miniature microscope objective for an endoscopic fiber confocal reflectance microscope," Appl. Opt. **41**, 4603-4610 (2002).
6. A. L. Polglase, W. J. McLaren, S. A. Skinner, R. Kiesslich, M. F. Neurath, and P. M. Delaney, "A fluorescence confocal endomicroscope for in vivo microscopy of the upper- and the lower-GI tract," Gastrointest. Endosc. **62**, 686-695 (2005).
7. G. J. Tearney, M. Shishkov, and B. E. Bouma, "Spectrally encoded miniature endoscopy," Opt. Lett. **27**, 412-414 (2002).
8. T. D. Wang, M. J. Mandella, C. H. Contag, and G. S. Kino, "Dual-axis confocal microscope for high-resolution in vivo imaging," Opt. Lett. **28**, 414-416 (2003).
9. D. Huang, E. A. Swanson, C. P. Lin, J. S. Schuman, W. G. Stinson, W. Chang, M. R. Hee, T. Flotte, K. Gregory, C. A. Puliafito, and J. G. Fujimoto, "Optical Coherence Tomography," Science **254**, 1178-1181 (1991).

10. G. J. Tearney, S. A. Boppart, B. E. Bouma, M. E. Brezinski, N. J. Weissman, J. F. Southern, and J. G. Fujimoto, "Scanning single-mode fiber optic catheter-endoscope for optical coherence tomography (vol 21, pg 543, 1996)," Opt. Lett. **21**, 912-912 (1996).

11. A. D. Aguirre, P. R. Herz, Y. Chen, J. G. Fujimoto, W. Piyawattanametha, L. Fan, and M. C. Wu, "Two-axis MEMS scanning catheter for ultrahigh resolution three-dimensional and en face imaging," Opt. Express **15**, 2445-2453 (2007).

12. S. H. Yun, G. J. Tearney, B. J. Vakoc, M. Shishkov, W. Y. Oh, A. E. Desjardins, M. J. Suter, R. C. Chan, J. A. Evans, I. K. Jang, N. S. Nishioka, J. F. de Boer, and B. E. Bouma, "Comprehensive volumetric optical microscopy in vivo," Nat. Med. **12**, 1429-1433 (2006).

13. D. Yelin, I. Rizvi, W. M. White, J. T. Motz, T. Hasan, B. E. Bouma, and G. J. Tearney, "Three-dimensional miniature endoscopy," Nature **443**, 765-765 (2006).

14. D. Yelin, S. H. Yun, B. E. Bouma, and G. J. Tearney, "Three-dimensional imaging using spectral encoding heterodyne interferometry," Opt. Lett. **30**, 1794-1796 (2005).

15. D. Yelin, W. M. White, J. T. Motz, S. H. Yun, B. E. Bouma, and G. J. Tearney, "Spectral-domain spectrally-encoded endoscopy," Opt. Express **15**, 2432-2444 (2007).

16. R. A. Leitgeb, C. K. Hitzenberger, A. F. Fercher, and T. Bajraszewski, "Phase-shifting algorithm to achieve high-speed long-depth-range probing by frequency-domain optical coherence tomography," Opt. Lett. **28**, 2201-2203 (2003).

17. J. T. Oh, and B. M. Kim, "Artifact removal in complex frequency domain optical coherence tomography with an iterative least-squares phase-shifting algorithm," Appl. Opt. **45**, 4157-4164 (2006).

18. M. Wojtkowski, A. Kowalczyk, R. Leitgeb, and A. F. Fercher, "Full range complex spectral optical coherence tomography technique in eye imaging," Opt. Lett. **27**, 1415-1417 (2002).

1. Introduction

Minimally invasive medical diagnosis and intervention are on the rise, owing in part to advances in the miniaturization of surgical instrumentation and optical imaging devices. Smaller and more flexible endoscopes are preferable in many applications in order to minimize tissue damage while the endoscope is inserted into the patient. Obtaining acceptable image quality in endoscopes with such small dimensions is challenging.

Subsurface imaging may also be important for some minimally invasive applications. Volumetric information can be beneficial by providing more diagnostic information, which is important for diseases that manifest below the tissue surface or require discrimination of surface from subsurface features for accurate diagnosis. For example, the degree of dysplasia in many epithelial cancers can be graded in part by determining of the extent to which the epithelia undergo surface maturation [1]. Also, during surgery, it can be helpful to see behind superficial tissues in the operative field, such as identifying blood vessels prior to surgical incision. Many minimally invasive operations are conducted through fluid; debris resulting from the procedure can cloud the field of view, making it difficult to subsequently identify the target. Finally, volumetric imaging provides perspective that can aid navigation and surgery, especially in confined spaces that may be traversed by a miniature endoscope [2].

Endoscopic confocal microscopy devices have been developed to look below tissue surfaces [3-8]. In general, these techniques utilize high numerical aperture objective lenses and confocal gating to reject out-of-focus light and allow optical sectioning of the tissue with subcellular resolution. However, these techniques suffer from relatively small fields of view and limited depth of field and working distance, making them not suitable for the navigation and macroscopic visualization roles of endoscopy.

Time-domain and Fourier-domain optical coherence tomography (OCT) also can be utilized for subsurface imaging inside the body. These methods rely on scanning a single optical beam to create a cross-sectional or volumetric image [9, 10]. Recently endoscopic Fourier-domain OCT has been utilized *in vivo* to also obtain large fields of view, albeit at volumetric frame rates of seconds to minutes [11, 12]. While promising for a wide variety of medical applications that require knowledge of subsurface information, OCT-based techniques are not capable of macroscopic imaging through miniature probes at real-time or video rates because the requisite rapid raster beam scanning mechanisms are too large to be incorporated within the confines of miniature endoscopes.

Spectrally encoded endoscopy (SEE) [7] is a recently developed technique that utilizes wavelength to encode transverse image information. The SEE probe, comprising a single optical fiber, a diffraction grating, and a low NA lens, focuses spectrally dispersed broadband light onto the sample. In turn, each point along this line is illuminated by a distinct spectral band. Each line of the image is acquired by measuring the spectrum of light reflected from the sample and returned back through the SEE probe using a high-speed spectrometer that resides outside the body. The second dimension of the image is obtained by moving the fiber at slow rates (e.g. 30 Hz). Without the need for rapid transverse scanning at the distal end of the endoscope, SEE allows video rate imaging to be performed through a miniature (i.e. 350 μm diameter) endoscopic device [13]. When the SEE probe is placed in the sample arm of an interferometer, it additionally can achieve three-dimensional topological, surface imaging in real-time, by use of time [14] and spectral [13, 15] domain low coherence interferometry.

In this paper, we extend the capabilities of SEE and demonstrate volumetric, sub-surface imaging of biological samples. To achieve volumetric imaging through a miniature endoscopic probe, we have designed a new detection setup that resulted with significant increase in sensitivity, redesigned the scanning in the reference arm for obtaining complex spectral measurements, and implemented new signal processing algorithms for extracting, unwrapping, and displaying the acquired volumetric data. We utilize this improved system to demonstrate subsurface imaging of a resolution target through 1 mm thick layer of intralipid, and volumetric imaging of a mouse embryo and an excised human stapes.

2. Experimental setup

In order to demonstrate subsurface imaging with SEE, a bench-top system (Fig. 1) was constructed and coupled to a 350 µm diameter spectrally-encoded endoscope [13]. Broadband light from a super-luminescent diode array (Superlum Diodes Ltd., Q870, center wavelength $\lambda_0 = 870$ nm, bandwidth $\Delta\lambda = 200$ nm) was coupled to the input port of a single-mode fiber optic Michelson interferometer after passing through a fiber-coupled circulator for isolation (OFR Inc.).
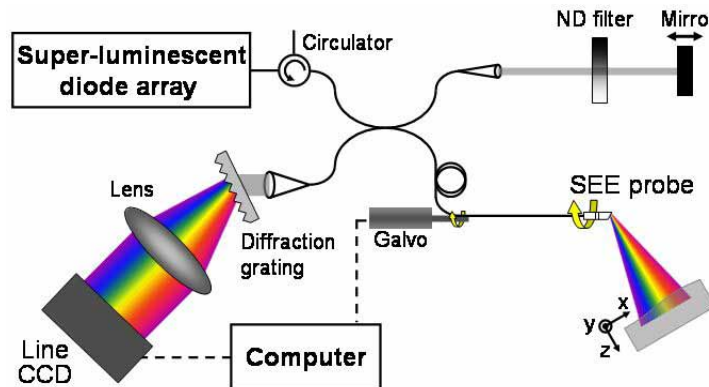

Fig. 1. Schematic of the spectrally-encoded endoscopy system. ND – neutral density; CCD – charge coupled device; SEE – spectrally encoded endoscopy.

A miniature endoscopic probe [13], comprising a single-mode optical fiber, a 350 μm diameter gradient index lens and a miniature transmission diffraction grating (1000 lines/mm), was used in the sample arm. The SEE probe formed a spectrally-encoded line (x-axis) on the surface of the sample. A galvanometric scanner was used for slow (y) axis scanning by rotating the probe, which was mechanically attached to the galvanometer shaft approximately 20 cm from its distal end. At the reference arm of the interferometer, a mirror on a piezo-driven translation stage was used to control the optical path length and a neutral density filter was used to adjust the reference power for optimization of the signal-to-noise ratio.

The spectrometer was improved compared to that of previous publications [13, 15] by utilizing a transmission diffraction grating instead of a reflective grating. Light was collimated using f = 50 mm collimating lens (OZ Optics limited). The collimated, 13 mm diameter beam illuminated a 1200 lines/mm volume phase holographic transmission grating (Wasatch Photonics Inc.). Diffraction efficiency exceeded 80% throughout the spectral range. The volume phase grating also had significantly lower polarization dependent loss. For SEE, a spectrometer with a transmission grating has several important advantages compared with reflectance grating spectrometer, including diffraction at Littrow's angle at the center bandwidth, resulting in improved wavelength linearity and easier alignment. Diffracted light was focused onto a high-speed linear 2048-pixel CCD array (Basler L104k-2k) using a wide aperture lens (Nikon, f = 85 mm, maximum aperture = 1.8). The camera was placed on a five axis aligner (New focus Inc.) that allowed independent translation and angular alignment. The camera and lens were mounted separately to allow tilting the CCD array in the plane of the spectral line and the optical axis in order to compensate for chromatic aberrations. The three dimensional volumetric data set was calculated from the spectral interference captured by the line CCD camera for different y-axis locations of the spectrally encoded line, $I(x_s,y)$, according to:

$$I(x_s, y, z) = \left| \frac{1}{\sqrt{W}} \int_{x_s - W/2}^{x_s + W/2} w(x'_s) \cdot I(x'_s, y) \exp\left(\frac{2\pi i x'_s \cdot z \cdot C_L}{W} \right) dx'_s \right|^2,$$ (1)

where x_s denotes the coordinate along the spectrometer's CCD array, W denotes the integration window size, $w(x'_s)$ denotes a window function (a rectangular window function, $w(x'_s) = 1$, was used in this work), and C_L is the coherence length associated with the bandwidth incident on each *transverse* resolvable point, which determines the axial resolution. Assuming an equal groove density for the two transmission gratings in the SEE probe and in the spectrometer, the transformation between the coordinate x and x_s is given by $x = x_s \cdot f_1 / f_2$, where f_1 and f_2 are the focal lengths of the probe and the spectrometer, respectively.

For situations where larger penetration is possible, or when the sample extends over substantial depth, the axial (z) range can be increased by a factor of 2 by placing the reference plane at the middle of the depth range and removing depth ambiguity. In a previous work [15], depth ambiguity was removed by computing the cross correlation between adjacent transverse lines, while slowly scanning the reference optical path. Applying this technique to every transverse plane within the volumetric data set was too slow to be performed in real time. We therefore utilized a phase shifting technique [16], which measures the complex spectrum by acquiring measurements of each sample location with two different reference phases. To accomplish phase shifting, we placed the reference mirror on a piezo-driven translation stage (Fig. 1) and applied a square wave at a frequency that was half the line rate. The amplitude of the transducer motion was adjusted to provide approximately $\pi/2$ phase difference between adjacent lines. Using two spectral measurements I_1 and I_2, the complex spectrum is given by:

$$I(x_s, y) = I_1(x_s, y) + \exp(i\Delta\phi(x_s)) I_2(x_s, y),$$ (2)

where

$$\Delta\phi(x_s) = P \cdot \frac{\lambda(x_s)}{\lambda^0} \cdot \frac{\pi}{2}.$$ (3)

Here, $\lambda(x_s)$ denotes the wavelength at location x_s, λ^0 denotes the central wavelength of the entire bandwidth, and P is a factor chosen in order to minimize phase errors due to reference scanning inaccuracies. In the current system, P was typically between 0.85 and 1.15, and was chosen to minimize image ghosts when the object covers only a half of the depth range.

Data was acquired in Labview 8.0 (National Instruments) using a PCI-1428 card. Processing in this development environment allowed the generation of integrated and surface x-y and x-z cross-sectional images at 5 frames per second. Volume rendering was conducted offline using Osirix 2.7.5.

3. Results

Using a 1951 USAF scattering resolution target, the transverse resolution was measured to be approximately 40 μm (group 3, element 5), and the field of view was 4.4 mm (working distance was ~13 mm), resulting in ~110 transverse resolvable points per spectrally encoded line. Each transverse resolution element contained a fractional bandwidth of approximately $\Delta\lambda/N_x = 1.8$ nm, corresponding to a theoretical axial resolution of 160 μm per pixel. We measured the axial resolution by performing a z-scan at the center wavelength. The actual resolution of the probe was found to be 180 μm, in good agreement with the theoretical value. Using a spectrometer with 2048 pixel camera (Basler L104k-2k, 10 μm pixel pitch), the spectrum from each resolvable point was measured by a 19 pixel window, resulting in an image depth range of 3.4 mm. With a total optical power on the sample of 0.82 mW, and at an imaging rate of 30 volumes per second, the detection sensitivity was measured to be 95 dB at the center of the field of view. The increase in sensitivity compared with previous SEE work (77 dB) [13] was made possible by the improved design and resolution of the spectrometer.

In order to demonstrate the ability of SEE to resolve features below highly scattering media, we placed a 1 mm thick glass cell filled with intralipid solution in front of the resolution target (Edmund Optics, Fluorescent standard resolution C57-792). This particular target was chosen since, compared with metal-coated reflectance targets, it better simulates tissue imaging, including more realistic scattering intensities and speckle characteristics. First, we imaged the resolution target through different intralipid concentrations while the reference arm was blocked. Compared with the image taken where the target was behind a clear solution (Fig. 2(a)), the image decayed rapidly with increasing concentrations and was barely detectable with 1% intralipid (Fig. 2(b)). The resolution chart was not visible through 2% intralipid (Fig. 2(c)). When the reference arm was deployed and spectral domain interferometry conducted [15], the signal-to-noise ratio was significantly enhanced, from ~10 dB in Fig. 2(a), to 30 dB (Fig. 2(d)). The resolution target was still clearly visible through 1% intralipid, with a signal-to-noise ratio comparable to Fig. 2(a), and with no apparent drop in resolution. The resolution chart could be fully visualized through 2% intralipid (Fig. 2(f)); with all group 2 elements resolved. Some fringe data loss, caused by occasional probe vibrations, was manifested by a few visible thin horizontal dark lines in Figs. 2(d-f).
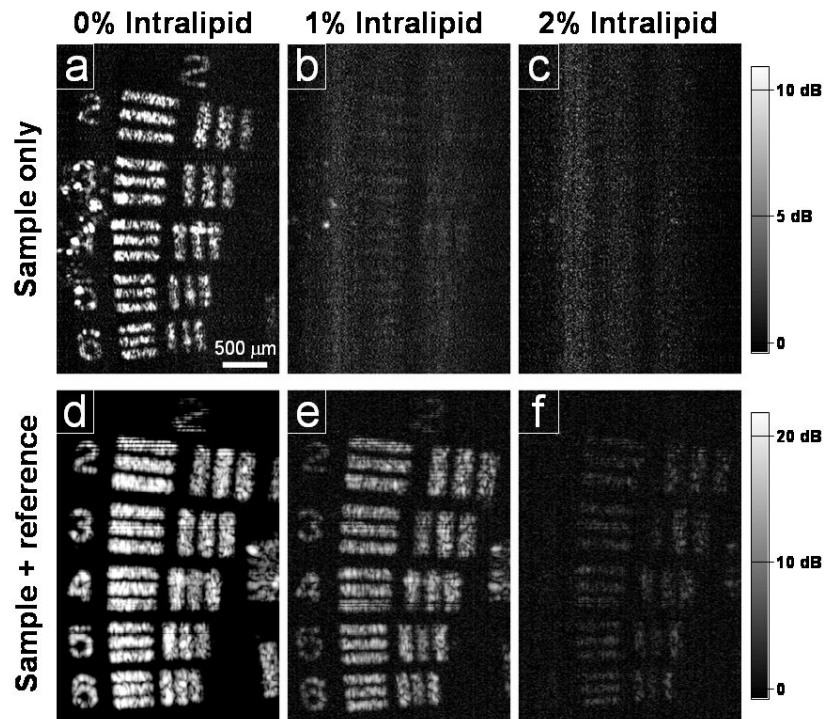
Fig. 2. Imaging of a scattering resolution target through a 1 mm thick layer of 0% (a), 1% (b), and 2% (c) intralipid with the reference arm blocked, is compared with imaging through the same concentrations (d-f) using spectral-domain interferometry. The width of the smallest bars in the resolution target (group 2, element 5) corresponds to approximately 79 μm. Images were plotted using a logarithmic look up table.

To demonstrate volumetric imaging of biological tissue we imaged the hind paw and tail of a formalin fixed mouse embryo at early developmental stage E14 (Fig. 3(a)). The mouse was contained in a plastic cuvette. Imaging was performed through the cuvette's 0.7 mm thick wall at a rate of 5 volumes per second. While the SEE system is capable of providing volume images at 30 Hz, this rate was chosen to avoid mechanical resonances in the probe that occurred at higher rates. The embryo's hind paw, umbilical cord, and the tail were clearly seen in the depth-integrated image shown in Fig. 3(b). A movie showing a series of lateral sections at depth intervals of 160 μm is provided in Fig. 3(c). The three-dimensional configuration of the anatomical structures are apparent in eight frames from the movie, shown in Figs. 3(d-j). The hind paw, the tail, and the umbilical cord are all clearly resolved in the sections d-k, including the gap between the paw and the tail (Fig. 3(i)), and a structure consistent with the tail ligament (Fig. 3(i), marked by arrow). Close inspection of the sections f and g reveals the phalanges as thin straight lines within the paw.
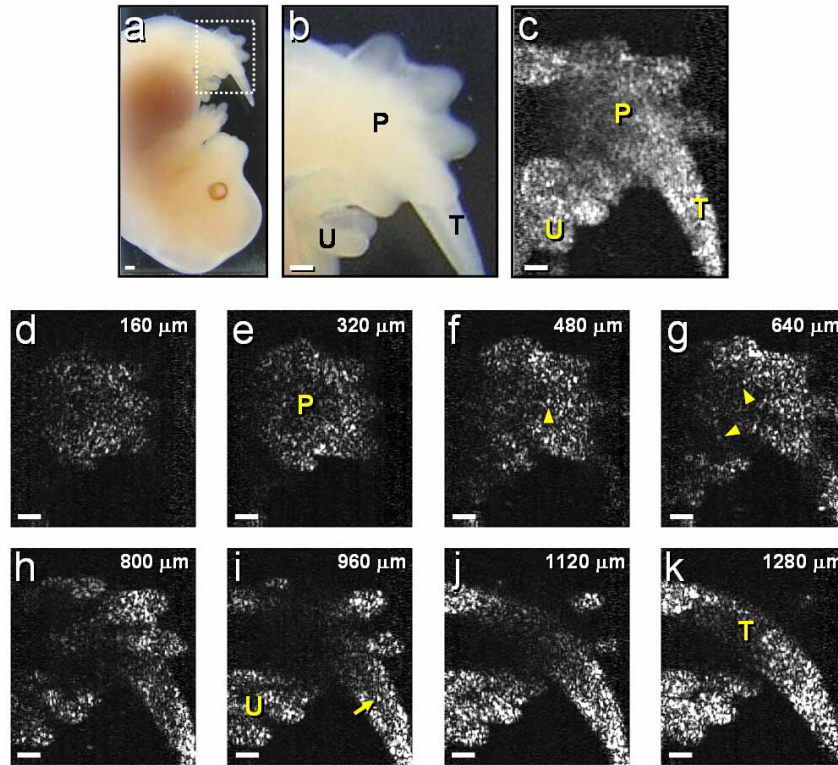
Fig. 3. (a) A photograph of a formalin fixed stage E14 mouse embryo. (b) A magnified view of the area within the dotted rectangle in (a). (c) Depth-integrated intensity image of the SEE volumetric data set shows the embryo's hind paw, tail and umbilical cord. (d-k) Transverse sections of the volume data set at different depths. The relative axial locations are shown in the upper right corner of each frame. Arrow heads in (f-g) mark the phalanges. Arrow in (i) denotes the tail ligament. P - hind paw. U - umbilical cord. T - tail. Scale bars represent 500 µm.

Endoscopic imaging of the middle ear is a potential application for SEE. One of the difficulties associated in imaging in small spaces such as the middle ear, is the lack of room to steer and navigate the probe. The ability to capture volumetric data behind the front surface may help in imaging areas that are hidden from the probe, thereby minimizing endoscope manipulation and potentially increasing safety and reducing procedure time. A volumetric rendering of an excised human stapes, one of the three ossicles of the middle ear, is shown in Fig. 4(b). This volume data set was acquired at a rate of 5 Hz and was captured without translation of the SEE probe (only probe rotation for y-axis scanning). Two x-z cross sections of the data set are shown in Figs. 4(c-d), revealing cross-sections of the bone at the locations marked in Fig. 4(b). The measured thickness of the stapes' posterior crus (labeled P) and anterior crus (labeled A) according to Fig. 4(c), are 600 µm and 420 µm for the left and right crura, respectively, in good agreement with caliper measurements of 620 µm and 360 µm. For comparison, a photograph of the stapes is shown in Fig. 4(a). Note that some three-dimensional structures near the foot plate are evident in the movie of the rendered data shown in Fig. 4(b).
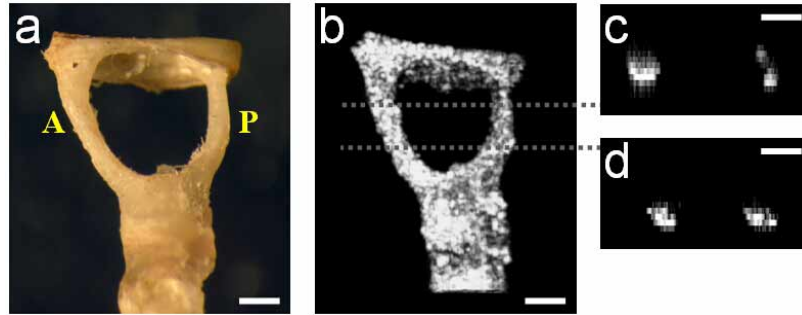
Fig. 4. (a) A photograph of an excised human stapes showing the anterior (A) and posterior (P) crura. (b) A movie showing volumetric rendering of the SEE data set. (c-d) x-z cross sections of the data set. A – anterior crus; P – posterior crus. Scale bars represent 500 µm.

The previous volume data sets of the embryo (Fig. 3) and the stapes (Fig. 4) did not extend over a depth that required the removal of depth ambiguity. To demonstrate volumetric depth unwrapping we imaged a larger field that contained the incudostapedial joint. For this field, the entire anatomical structure extends over 3 mm in depth. A rendered depth-integrated SEE image is shown in Fig. 5(a). The shape and structure of the stapes, the incus, and the joint are clearly visible in this image. A photograph obtained at a similar orientation is shown in Fig. 5(b) for reference.
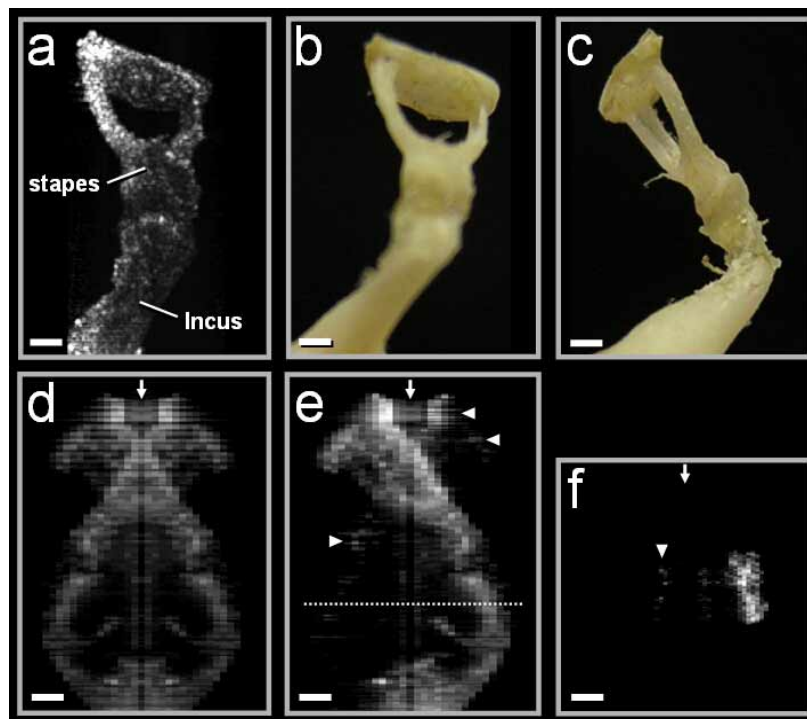

Fig. 5. (a) Depth-integrated rendered SEE image of excised human ossicles, showing the stapes, incudostapedial joint and incus. (b) A photograph of the bones in a similar orientation to (a). (c) A photograph showing a side view of the incudostapedial joint. (d) Projection of the data set on the y-z plane. The image is wrapped around the reference plane (marked by an arrow). (e) The unwrapped y-z image, shows the full extent of the joint. (f) An x-z cross section of the data set at the location marked by dotted line in (e). Arrows in (d-f) mark the location of the reference plane (e). Arrow heads in (e) and (f) mark ghosting artifacts due to errors in depth ambiguity removal. Scale bars represent 500 µm.

A side view photograph (Fig. 5(c)) shows that the imaged object extends about 2.85 mm in depth (z axis). Projections of the data set on the y-z plane that were obtained before applying data unwrapping demonstrate the expected symmetrical image around the reference plane (Fig. 5(d)). The unwrapped image that was computed from the short-time Fourier transform of the complex spectrum is shown in Fig. 5(e) and reveals the nearly right angle bending of the incus close to the joint. An x-z cross section of the data corresponding to the section marked by a dotted line in (e) is shown in Fig. 5(f). Faint ghost image data around the reference plane (marked by arrow heads) is evident, resulting from errors in the depth ambiguity removal process. Imaging was performed at a rate of 5 volumes per second.

4. Discussion

Conventional wide-field endoscopes are incapable of visualizing below the tissue surface. SEE uses low coherence interferometry to obtain volumetric imaging with sufficient resolution and sensitivity to image subsurface structures while maintaining the large field of view required for endoscopy.

The spectral domain SEE (SD-SEE) presented in this work and in Ref. [15] shares some common features with spectral-domain OCT (SD-OCT), including the use of a high-speed, high-resolution spectrometer to capture spectral interference. Table 1 summarizes the main differences between SD-SEE and SD-OCT.

Table 1. Differences between spectral domain SEE (SD-SEE) and spectral-domain OCT (SD-OCT).

	SD-SEE	**SD-OCT**
Imaging optics	Lens, diffraction grating	Lens
Single capture	x-z plane	'A-line' (z axis)
Transverse scanning	1 axis	2 axes
Depth resolution	A few hundred microns	A few microns
Data processing	Short-time Fourier transformation	Full spectra Fourier transformation

The data at each transverse location of the SEE image is essentially equivalent to a single SD-OCT A-line, but with bandwidth that is smaller by a factor that equals the number of resolvable point per spectrally encoded line. As a result, SD-SEE has poorer axial resolution, but is much less sensitive to the effect of dispersion and geometrical nonlinearities caused by the diffraction grating of the spectrometer. More importantly, SD-SEE is capable of obtaining wide-field volume images at video rates, through endoscopes that have diameters that are as small as the optical fiber itself.

In this demonstration, probe vibrations and optical power were the main limiting factors of subsurface imaging. Power and vibrations were less limiting in previous works [13, 15], since surface reflections were considerably stronger than subsurface signals, and data processing algorithms were simpler and more robust. At imaging speeds below 4 volumes per second, long exposure times (0.5-5 ms) allowed for high signal-to-noise ratios, but also resulted in high susceptibility to occasional probe vibrations and sample movements. At 20-30 volumes per second we noticed a reduction in image quality due to vibrational resonances in the flexible probe, as well as limited penetration depth due to the shorter exposure times (66-100 μs). At ~5 volumes per second, image quality was optimal. In this work, the optical power on the sample was 0.82 mW, which is much lower then the ANSI standards for skin. We anticipate that penetration depths could be doubled in some cases, using higher powers on

the sample. Laser powers of a few tens of milliwatts are achievable today with commercially available Ti:sapphire oscillators and continuum sources.

Probe vibrations often induce phase fluctuations between adjacent lines (spectra), resulting in image artifacts originating from the depth unwrapping process. A possible solution includes positioning the reference plane above the tissue surface, eliminating the vibrations artifacts; however, depth range is reduced to half. Other approaches for reducing phase instability artifacts include more sophisticated data acquisition and processing algorithms by acquiring more image data with different reference phases [17, 18]. These approaches could be adapted and applied to SEE to reduce ghosting artifacts and improve image quality.

In addition, future designs of the endoscopic probes could reduce vibrations by improving mechanical stability and utilizing different probe and sheathe materials. Applying alternative scanning methods, such as full probe rotation instead of the current raster scanning approach, could also improve stability and increase the field of view. We anticipate that by increasing sample power and by improving probe design and construction, volumetric imaging with minimum artifacts should be feasible at video rate.

Acknowledgments